1   Revision 1

2   Word count: 10025 of which 7229 in Abstract – Implications

3   **Clustering and interfacial segregation of radiogenic Pb in a mineral host – inclusion system**

4   **Tracing two-stage Pb and trace element mobility in monazite inclusions in rutile**

5   R. Verberne[1, 2, 3]* (0000-0002-5529-1250), Steven M. Reddy[2,3] (0000-0002-4726-5714), Denis

6   Fougerouse[2, 3] (0000-0003-3346-1121) , Anne-Magali Seydoux-Guillaume[5] (0000-0002-9921-4695),

7   David W. Saxey[2, 3] (0000-0001-7433-946X), William D.A. Rickard[2] (0000-0002-8118-730X), Zakaria

8   Quadir[4] (0000-0003-1626-3748), Chris Clark[3] (0000-0001-9982-7849)

9   [1]Centre for Star and Planet Formation, Globe Institute, University of Copenhagen, Øster Voldgade 5–7,

10   DK-1350 Copenhagen, Denmark;

11   [2]Geoscience Atom Probe, John de Laeter Centre, Curtin University, Perth, WA 6845, Australia.

12   [3]School of Earth and Planetary Sciences, Curtin University, Perth, WA 6845, Australia

13   [4]Microscopy and Microanalysis Facility, John de Laeter Centre, Curtin University, GPO Box U1987,

14   Perth, WA 6845, Australia

15   [5]UJM-Saint-Etienne, LGL-TPE UMR5276 CNRS, 42023 Saint-Étienne, France *Correspondence:

16   E-mail: rick.verberne@sund.ku.dk; rick.verberne89@gmail.com

Abstract

17

18 Accessory minerals like zircon, rutile and monazite are routinely studied to inform about the timing and

19 nature of geological processes. These studies are underpinned by our understanding of the transfer

20 processes of trace elements and the assumption that the isotopic systems remain undisturbed. However,

21 the presence of microstructures or Pb-bearing phases in minerals can lead to the alteration of the Pb

22 isotopic composition. To gain insight into the relationship between Pb isotopic alterations from inclusions

23 and microstructures, this study focused on inclusions from an ultra-high temperature metamorphic rutile.

24 The studied inclusions are submicron monazites, a common mineral rich in Pb but normally not present in

25 rutile. The sample is sourced from Mt. Hardy, Napier Complex, East Antarctica, an ultra-high

26 temperature (UHT) metamorphic terrane. By applying correlative analytical techniques including electron

27 backscatter diffraction mapping, transmission electron microscopy (TEM), and atom probe tomography, it

28 is shown monazite inclusions are often in contact with low-angle boundaries and yield no preferred

29 orientation. TEM shows the monazite core has a mottled texture due to the presence of radiation damage

30 and nanoclusters associated with the radiation damage defects that are rich in U, Pb, and Ca. Some

31 monazites exhibit a core-rim structure. The rim yields clusters composed of Ca- and Li-phosphate that

32 enclose Pb nanoclusters that are only present in small amounts compared to the core, with Pb likely

33 diffused into the rutile-monazite interface. These textures are the result of two-stages of Pb mobility.

34 Initial Pb segregation was driven by volume diffusion during UHT metamorphism (2500 Ma). The second

35 stage is a stress-induced recrystallization during exhumation, leading to recrystallization of the monazite

36 rim and trace element transport. The isotopic signature of Pb trapped within the rutile-monazite interface

37 constrains the timing of Pb mobility to c. 550 Ma.

38

39 **Keywords:** Rutile, Monazite, Pb mobility, Atom Probe Tomography

Introduction

40

41   Rutile (TiO_2) is a common accessory mineral that is stable at mid- to lower-crustal metamorphic

42   conditions (Clark et al., 2019; Dachille et al., 1968; Harley, 2016). Zr-in-rutile geothermometry and rutile

43   U-Pb geochronology are increasingly used to provide temperature and time constraints on the evolution of

44   metamorphic terranes (Clark et al., 2018; Kooijman et al., 2010; Meinhold, 2010; Smye and Stockli,

45   2014; Watson et al., 2006; Zack et al., 2004a). Mineral inclusions in rutile are geologically significant

46   with inclusions of corundum in rutile providing constraints on growth mechanisms (Daneu et al., 2014),

47   whilst the molar fraction of Zr-bearing mineral inclusions can be used to re-integrate Zr concentrations

48   for the estimation of peak metamorphic temperatures (Mitchell and Harley, 2017; Pape et al., 2016). The

49   ability of rutile to trap and isolate inclusions from retrograde metamorphic overprints and fluid alteration

50   events may allow inclusion assemblages in rutile to be used to characterize metamorphic conditions in

51   ultra-high pressure (UHP) and ultra-high temperature (UHT) metamorphic terranes (Hart et al., 2016;

52   Hart et al., 2018).

53   Despite the uses of inclusion analyses, the presence of small (<1 μm diameter) inclusions in rutile has the

54   potential to compromise compositional and isotopic analysis of the host mineral by techniques, such as

55   Laser ablation inductively coupled plasma mass spectrometry (LA-ICP-MS), which analyses significantly

56   larger volumes than the inclusion volume. Little is currently known about the geochemistry of sub-

57   micrometer mineral inclusions or how their presence and composition may affect the analysis of the host.

58   In part, this reflects the difficulty in measuring the trace element and isotopic compositions of such small

59   inclusions. Furthermore, there is little information regarding how such inclusions may evolve as the

60   pressure-temperature conditions of the host rock change over time, or if such inclusions are truly isolated

61   from the matrix of the rock in which the host mineral resides. In this contribution, the structural setting

62   and compositional character of micrometer-scale (200-1100 nm) monazite inclusions within ultra-high

63   temperature metamorphic rutile are studied to provide some constraints on host-inclusion relationships

64   and determine the mechanisms by which compositional heterogeneity in the inclusion may be developed.

65   The mobility of Pb in monazite has received significant attention in nanoscale studies using transmitted

66   electron microscopy (TEM) and atom probe tomography (APT) (Bingen and Van Breemen, 1998;

67   Fougerouse et al., 2021a; Fougerouse et al., 2018; Grand'Homme et al., 2016; Seydoux-Guillaume et al.,

68   2003; 2012; 2019; Turuani et al., 2022, 2023). However, such studies have typically analyzed the internal

69   parts of large monazite crystals, ignoring the potential complications associated with Pb mobility adjacent

70   to mineral-mineral interfaces that characterize small inclusions.

71   The complementary use of APT, TEM and electron backscattered diffraction (EBSD) provides unique

72   insight into Pb migration within the inclusions (Reddy et al., 2020). The results obtained show evidence

73   for multiple mechanisms of Pb and trace element mobility, provide important insights into the segregation

74   of Pb to mineralogical grain boundaries and yield important new observations that influence the

75   interpretation of isotopic data from sub-micrometer monazite grains in a mineral – host system.

76

77   **Geological setting and sample description**

78   The sample used for this study was collected from Mt Hardy in the Napier Complex of East Antarctica

79   (Fig. 1a) and is from an Archean Mg-Al rich metapelitic layer. The Napier Complex consists of a suite of

80   Archean (2990 – 2800 Ma, Black, Williams, & Compston,

81   1986 Harley & Black, 1987. ortho- and paragneisses that underwent a complex deformational and

82   metamorphic history including two ultrahigh temperature (UHT) metamorphic events at c. 2850 and c.

83   2580 Ma with their timing constraint by zircon dating. (Clark et al., 2018; Harley, 2016; James and Black,

84   1981; Sheraton et al., 1987). The c. 2500 Ma UHT event is widely believed to have resulted in the

85   formation of the highest regional-scale temperatures for exposed crustal rocks on Earth, with temperature

86   estimates, coming from the region where Mt Hardy is located, of between 1050–1120 °C (Harley and

87   Motoyoshi, 2000; Hokada, 2001). These high temperatures are thought to have persisted for in excess of

88   100 Myr (Clark et al., 2018; Harley, 2016). Two younger events, mostly in the southern region of the

89   Napier Complex have been described by Black et al. (1983); Black et al. (1984). Zircon and monazite U-

90   Pb dating constrain an amphibolite-facies metamorphic event to take place between 1073-1094 Ma. Rb-Sr

91   ages record new magmatic and hydrothermal activity to take place around 522 Ma (Black et al., 1983). A

92   study on galena inclusions in monazite (Turuani et al., 2022) shows the latter event (522 Ma) was more

93   localized while the event at 1073 Ma was more pervasive within the Napier Complex.

94   The sample is comprised of dry residual layers of porhyroblastic garnet–cordierite–spinel–sapphirine–

95   osumilite (now replaced by symplectites of K-feldspar–cordierite–dendritic orthopyroxene) and quartz–

96   mesoperthite leucosomes (Fig. 1b). Rutile occurs as inclusions in garnet and within both the residual

97   layers and leucosomes, rutile is inferred to form part of the peak UHT assemblage. In this sample, a

98   population of sector zoned "soccer-ball" type zircons interpreted to be metamorphic in origin yielded a

99   concordia age of 2492 ± 7 Ma and a Ti-in-zircon temperature of 915 ± 30°C (Clark et al., 2018). The

100   monazite inclusions reside in two rutile grains. The monazites studied were extracted from rutile in direct

101   contact with garnet, mesoperthite, and traces of biotite. Submicron monazite inclusions are also present in

102   the biotite present in the direct vicinity of the rutile grain of interest. No large monazite grains are present

103   within this sample. However, the earliest monazite in the Napier complex likely crystallized around 3070

104   Ma (Black et al., 1984).

105

106   **Methods**

107   **Electron backscatter diffraction & electron dispersive X-ray spectroscopy**

108   The thin section has previously been analyzed by LA-ICP-MS. Following LA-ICP-MS, the thin section

109   was re-polished and carbon-coated and analyzed by SEM. SEM characterization was undertaken on a

110   TESCAN Mira3 field emission scanning electron microscope housed at the John de Laeter Centre (JdLC),

111   Curtin University, Perth, Australia and included electron backscatter diffraction (EBSD) and energy-

112   dispersive x-ray spectroscopy (EDS) mapping. Analyses were undertaken with an accelerating voltage of

113   20 kV and an instrument specific 'beam intensity' of 17 using a working distance of 20 mm and 70°

114   specimen tilt. For mapping of rutile, a 500 nm step size was used and the match units for rutile were

115   obtained from the American Mineralogist crystallography database (801 448-45x) (Swope et al., 1995).

116   Match units for monazite were derived from the crystallographic data of (Ni et al., 1995), following

117   (Erickson et al., 2015). EBSD mapping of the monazite inclusions was done using a 50 nm step size.

118   Post-processing of EBSD data was performed in Matlab®, version R2022b, with the free toolbox MTEX

119   Version 5.8.2 (Bachmann et al., 2010). Images are constructed using local misorientation and the mean

120   misorientation of the rutile grain. The maps were plotted using the 'roma' scientific color map (Crameri,

121   2018). Post-processing involved a noise-reduction by removal of groups of <5 adjacent pixels ('Wild'

122   spikes/shards) with crystal orientations within 10° of those of their neighbors. The procedure was

123   followed by applying a 5×5 pixel median filter. The filter smooths the orientations in the EBSD data

124   while preserving subgrain boundaries. Slip system characterization was undertaken following established

125   methodologies (Lloyd et al., 1997; Prior et al., 2002; Reddy et al., 2007).

126

Focused-ion-beam SEM and TEM

128   Analysis by transmission electron microscope (TEM) and atom probe tomography (APT) requires

129   samples to be prepared in the form of electron-transparent thin foils (TEM) or needle-shaped specimens

130   (APT). These samples were prepared at two different institutes.

131   **Curtin University.** TEM and APT specimens analyzed at Curtin University were prepared on a

132   Tescan Lyra3 Ga Focused-Ion Beam Scanning Electron Microscope (FIB-SEM), housed in the John de

133   Laeter Centre, Curtin University. The Tescan Lyra3 comes equipped with an electronically operated

134   nanomanipulator and Pt gas injection system. The FIB was operated with an accelerating voltage of 30

135   kV for the monoisotopic (mass 69 Da) Ga^{+}-source. For backscatter electron (BSE) imaging in SEM-

136   mode, an accelerating voltage of the electron beam was varied between 5, 10 & 20 kV to provide a depth

137   control on the size of the monazite inclusions below the surface. All, TEM and APT, specimens were

138   extracted from one, out of the two, grains that contained monazite inclusions.

6

139   The TEM foil was prepared by cutting a vertical slice using the FIB and lifted out using the

140   nanomanipulator. The TEM foil was mounted on a copper half-grid and thinned until electron transparent

141   (< 100 nm) followed by a 2 kV clean-up routine to remove damage and Ga implantation caused by the 30

142   kV ion beam. After initial imaging by TEM, the sample was further thinned to 30-50 nm to reduce the

143   curvature effect of the inclusion during Scanning TEM (S/TEM) EDS.

144   **Jean Monnet University (UJM).** One TEM foil was prepared using a Thermo Fisher Scientific

145   FEI 125 Helios Nanolab 600i focused-ion beam scanning electron microscope (FIB/SEM) hosted by the

146   MANUTECH USD platform in Saint-Etienne (France). Before extraction of the sample, the area of

147   interest is protected with a 1 μm carbon coat. A 30 kV 10 nA Ga-ion beam is used to cut out the foil

148   (15x10x1 μm). The foil is then lifted out and deposited on a Cu half-grid, thinned with an ion beam until

149   ~ 100 nm thickness, and then "cleaned up" at low voltage (2 kV) to remove the amorphous part, resulting

150   in a sample ~60 nm thick.

151

Transmission Electron Microscopy

153   TEM analysis at Curtin University was performed on the FEI Talos FS200X Field Emission Gun TEM

154   equipped with a Super-X EDS detector housed in the John de Laeter Centre. The TEM was operated at

155   200 kV. TEM imaging was conducted in both bright and dark field (BF and DF) modes. The TEM

156   diffraction investigation was conducted with the assistance of Kikuchi patterns that were generated with

157   the convergent beam electron diffraction (CBED). A small spot was used to minimize the beam related

158   damages to the sample, and the sample was tilted to the right diffraction zone axis or two-beam condition

159   to acquire selected area diffraction (SAD) patterns. Both BF and DF TEM imaging were undertaken with

160   the objective apertures after tilting the sample to a diffraction condition within 20°. TEM, STEM, and

161   EDS data acquisition were conducted with the Velox software.

162   Chemical analysis was done by the attached two pairs of super X detectors. The TEM is fitted with four

163   scanning transmission electron microscopy. (STEM) detection systems: High Angle Annular Dark Field

164   (HAADF), upper Dark Field (DF4), lower Dark Field (DF2), and BF. The contrasts in HAADF are

7

165 predominantly made from chemical/phase differences and the contrast in BF is predominantly made from

166 orientation differences. The DF4 and DF2 detectors reveal both chemical and orientation contrasts at

167 different levels.

168 EDS data was acquired with a beam current of 0.6 nA and collected over 45-90 min for each presented

169 map.

170 HAADF TEM images provide information based on atomic number (Z) contrast with high z values being

171 brighter.

172 TEM characterization in UJM Saint-Etienne was performed with a Cs-corrected TEM (NeoARM200F

173 Cold FEG) operated at 200 kV, operated by the CLYM (Consortium Lyon Saint-Etienne de Microscopie)

174 and hosted within the Hubert Curien Laboratory. The instrument is equipped with a wide-angle energy

175 dispersive X-ray (EDX) spectrometer SDD CENTURIO-X from JEOL, two STEM detectors (annular

176 dark field and annular bright field from JEOL and Gatan) with a CMOS camera Gatan Rio (4kx4k), a

177 CCD camera Ultrascan from Gatan (2kx2k), and an electron energy-loss spectrometer (EELS) (Gatan GIF

178 Quantum ER). The resolution in STEM at 200 kV is 0.78 Å due to the presence of a Cs corrector CEOS

179 ASCOR.

180

181 **Sample preparation for atom probe tomography**

182 For the preparation of APT specimens, monazite was marked by depositing Pt buttons in the middle of

183 the targeted inclusion prior to the deposition of a protective layer (Rickard et al., 2020). APT specimen

184 preparation followed lift-out and sharpening procedures described elsewhere (Rickard et al., 2020;

185 Thompson et al., 2007). A wedge-shaped sample was cut using the ion beam at an angled surface and

186 lifted out using a nanomanipulator. The wedge was brought to the APT specimen holder consisting of a

187 coupon with 22 silicon posts to hold the specimens. The wedge was aligned over the top of a silicon post

188 and a segment was attached using ion beam deposition with a Pt precursor. The wedge above the post was

189 cut leaving ±2 μm of sample on the silicon post. This process is repeated until all material in the wedge

190 has been placed on posts. Following the mounting of specimens on the silicon posts, the specimens were

8

191   then sharpened using an annular milling technique until needle-shaped specimens approximately 2.5 μm

192   in length and less than <100 nm wide at the tip were formed. This was followed by a 2 kV clean-up

193   routine to remove the damaged layer. All specimens were imaged by secondary electron (SE) and

194   backscatter electron imaging (BSE) imaging in SEM-mode only at a working distance of 6 mm and an

195   accelerating voltage of 10 kV.

196

197   **Atom probe tomography**

198   APT analyses were conducted at the Geoscience Atom Probe Facility, Curtin University. This system is a

199   Cameca Local Electrode Atom Probe (LEAP) 4000X HR that allows laser-assisted field evaporation and

200   high mass-resolving power. Data were collected using a 125 kHz pulse rate, a laser pulse energy of 100

201   pJ, a base temperature of 70° K and an ion detection rate of 0.3% based on (Fougerouse et al., 2018;

202   Verberne et al., 2019). Post-processing was done using Cameca's Integrated Visualisation and Analysis

203   Software (IVAS) 3.8.0. Reconstructions are based on the density of rutile and using the shank-angle

204   reconstruction mode because of the poly-phased nature of our region of interest (Fougerouse et al.,

205   2021c).

206   Atoms are evaporated as both single ions and molecular species with a range of different ionization states.

207   Peaks in the mass spectra were labelled per individual isotope for specific ionization states and ranged

208   with a constant width of 0.2 Da. For visualization and compositional analyses, isoconcentration surfaces

209   (Hellman et al., 2000) were computed in IVAS using 1-2 at% for the respective element of interest. These

210   isoconcentration surfaces can be used to isolate each of the individual phases in the datasets. System

211   details, reconstruction parameters and other experimental conditions are summarized in (DR-1) following

212   the recommendation of (Blum et al., 2018a). $^{207}Pb/^{206}Pb$ ratios are calculated with corrections for

213   background levels and thermal tails. Pb in these samples can be detected at two different ionization states,

214   Pb^+ and Pb^{++}, and corrections are needed to account for the $^{206}Pb^{++}$ (103 Da) peak tail on the $^{207}Pb^{++}$

215   (103.5 Da) peak, but also $P_3O_7^+$ (205 Da) on $^{206}Pb^+$ (206 Da) and $^{206}Pb^+$ (206 Da) on $^{207}Pb^+$ (207 Da).

9

216   Measurement of isotopic ratios was undertaken using a range of different peak widths and bin sizes

217   following (Blum et al., 2018b).

218   From the prepared submicron monazites specimens (n=11), APT analysis resulted in three successful

219   runs, with a respective yield of 70, 45, and 9 million detected ions. The analysis of interfaces provides a

220   challenge as the interface is a weak spot in the material. The 3D reconstructions show that in all

221   specimens the monazite is encapsulated within rutile indicating that only the rim of the monazite

222   inclusions was analyzed. Monazites not encapsulated by rutile in the APT specimen likely delaminated

223   during the analysis. The datasets were evaluated by generating isoconcentration surfaces that subdivide

224   the specimens into three components - rutile, monazite and the interface. This allowed for the separate

225   interpretation of the mass spectra of each component.

226

227   **Results**

228   **Petrography and analysis of the rutile host**

229   The studied rutile grain occurs in a rock consisting of residual layers and leucosomes. Monazite

230   inclusions are found in two rutile grains within this thin section, as well as in the directly surrounding

231   biotite (Fig. 2b, c). No monazite inclusions were found in the garnet or mesoperthite. The rutile grain

232   studied is approximately 250 x 200 μm in size, with at least 46 sub-micron monazite inclusions visible at

233   the surface. EBSD mapping of individual monazite grains shows no evidence for a crystal-preferred

234   orientation of the inclusions in either the rutile or the surrounding biotite (fig 2d).

235   Several different microstructures are revealed by EBSD mapping. Twin boundaries are observed in two

236   orientations corresponding to a 65° rotation and belong to the {101} <100> twin relationship. In addition,

237   a network of low-angle boundaries (Fig. 2d, e) is visible. The low-angle boundaries have a misorientation

238   axis of (010), with the dispersion of 1-2°, corresponding to the {101}<201> slip system (Fig 2e). The

239   LAB are straight (LAB 1) or bent around the monazite inclusions (LAB 2).

240   **Atom probe observations of the rutile host.** Fe and Zr, which are common trace elements in

241   rutile, are detected within the mass spectra. U and Pb are not observed above the background (Fig 6). In

242   the 3D reconstruction, no heterogeneities can be observed within the rutile matrix this includes ranging

243   the theoretical U and Pb peaks. The rutile mass spectra are comparable to those obtained during previous

244   APT studies of rutile e.g., (Verberne et al., 2019; Verberne et al., 2023).

245

246   **Structural and chemical analysis of the monazite inclusions**

247   The examination of two TEM thin-foils, both incorporating a single monazite inclusion, indicates

248   variations in the texture and chemical associations of the outer rim of monazite in the two inclusions. In

249   one monazite, there is a clear core-rim structure (Fig 3). In contrast, the second monazite inclusion only

250   records the 'core' structure throughout the entire inclusion (Fig 4). In both monazites, the core has a high

251   density of clusters, while the rim structure has a lower density of clusters but this records a discrete

252   compositional variation (Fig 4, 5).

253   Trace elements observed within the monazite APT mass spectra (Fig. 6) include Ca^{++} (20 Da), Mg^+ (24

254   Da) and Li^+ (6 Da). ^{238}U was detected as $^{238}UO_2^{++}$ at 135 Da and no peak was present for $^{235}UO_2^{++}$. Pb in

255   monazite is observed with two different ionization states: $^{206}Pb^+$ and $^{207}Pb^+$ (206 and 207 Da) as well as

256     $^{206}Pb^{++}$ and $^{207}Pb^{++}$ (103 and 103.5 Da). $^{208}Pb^+$ and $^{208}Pb^{++}$ were not observed above the background.

257   Furthermore, no Th-bearing species were identified within the mass spectrum.

258   **Chemical heterogeneities in the monazite core.** The inner region of the monazite exhibits a

259   mottled texture identifiable in BF mode (Fig. 4). In one monazite, this texture is only present in the core-

260   region, whereas this texture is present throughout the second monazite grain imaged by TEM. The

261   mottled texture is due to the presence of dark (in BF mode) and bright (in DF mode) spots. These reflect

262   radiation damage and crystal defects as well as nanoclusters ± 5 nm in size. STEM-EDS revealed some of

263   these nanoclusters are composed of trace elements (U, Pb, and Ca) (Fig. 7a, b).

264   **Trace element distribution in the monazite rim.** This rim is only visible in one of the two

265   imaged monazites (Fig 4b). The monazite rim is ~100 nm wide. Here, the matrix of the monazite appears

266   pristine while hosting several nanoclusters 20-30 nm in diameter (Fig 5). Lattice imaging of the clusters

267   shows a continuous lattice consistent with monazite (Fig 5d-f). Here, we differentiate between a cluster

268 and inclusion based on similar properties as mentioned in Turuani et al., 2023. The presence of a grain

269 boundary is indicative of an inclusion while a continuous lattice/absence is an indication of a cluster. The

270 clusters in the monazite consist of two types of darker clusters as seen in the HAADF images (Fig 4b, 7c,

271 d) and sometimes encompass one or two bright spots. One type of darker cluster was shown to be rich in

272 Ca (Fig 7c). However, the second type of nanocluster did not yield an EDS response. This indicates the

273 major constituents of this cluster may have an atomic number that is too low for S/TEM-EDS ($< Z = 6$).

274 Alternatively, this could point to a void and represent porosity within the cluster. The bright spots within

275 both these clusters yielded an increased concentration of Pb (Fig. 7c).

276 The 3D reconstruction of the monazite APT reveals two types of clusters in the monazite rim (Fig. 8). The

277 first type is dominated by Ca. These clusters have a diameter of 20-30 nm containing up to 10 at. % Ca

278 (Fig. 9). Ca-rich inclusions are often accompanied by an increase in Pb of up to 2-3 at. % as well as Y, up

279 to 1.2 at. %. However, not all Ca-rich inclusions show an increase in the Pb signal. The increase in Ca and

280 other trace elements is compensated by a depletion in REE and O with P remaining relatively constant. Pb

281 is spread over four peaks within the mass spectrum, resulting in insufficient counts for meaningful

282 determination of $^{207}Pb/^{206}Pb$ ratios after correcting for the static background and the tails of the preceding

283 peaks. Therefore, despite the presence of Pb within the inclusion, no isotopic composition could be

284 obtained.

285 The second inclusion type is enriched in Li^+, with values up to 30 at. % Li (Fig. 9). These inclusions are

286 ~20 nm in diameter. Li-rich inclusions have Pb concentrations up to 0.6 at. % and therefore incorporate

287 less Pb than the Ca-rich inclusion, yet have elevated levels compared to the monazite matrix. Like the Ca-

288 rich inclusions, the increase of Li and traces is compensated by a depletion in REE and O with P

289 remaining at roughly 10 at. %. (Fig. 9). Pb isotopic compositions could not be obtained from the Li-

290 inclusions for similar reasons as with the Ca-inclusions.

291

292 **The rutile-monazite interface**

12

293   The interface between rutile and monazite inclusion is sharp and coherent (Fig 4a). Chemical mapping of

294   the interface by TEM shows the enriched zone in the interface between the rutile and monazite is

295   approximately 2 nm wide at the narrowest part of this boundary.

296   STEM-EDS analysis was applied to further characterize the different features present within the

297   monazite. The interface between rutile and monazite with core-rim texture yields 2-4 at. % Pb based on a

298   line profile across the interface (Fig. 7d) and with no signals above the detection limit for other trace

299   elements.

300   The mass spectra obtained from the interface show components of both the monazite and rutile mass

301   spectrum. The boundary is enriched in trace elements including U, Pb, Ca, Li, Mg, Si and Al. Ca and Pb

302   concentrations reach 2-3 at. % in all three specimens. The trace element distribution at the interface of

303   specimen 3 is heterogeneous, most clear for trace elements with a lower overall concentration, e.g. Si and

304   Al (Fig. 10), but similar distributions can be observed for Pb (Fig. 10).

305   The heterogeneous distribution of trace elements in the interface of specimen 3 is visualized in the

306   reconstruction and measured along a 1d profile (fig 10). The combined concentrations of Al + Si are

307   shown and a contrast in concentration is visible from the apex of the tip to the lower part of the

308   reconstructed volume. The transition from low to higher concentration is accompanied by linear features

309   enriched (labelled A, B, and C) in trace elements. Additionally, clusters of Mg are present at this

310   interface. These clusters contain up to 20 at. % Mg and have a Ca concentration of ~4 at% (Fig. 9), which

311   is higher than the average concentration within the interface. The width of the interface was estimated to

312   be ~8 nm based on the Pb concentration profile.

313

314   **Pb isotopic compositions of interfacially segregated Pb**

315   The mass spectra of the interface between rutile and monazite show ^{206}Pb and ^{207}Pb are present as both

316   Pb$^+$ and Pb^{++}. The 3D reconstruction shows the Pb is homogeneously distributed along the interface of

317   specimens 1 and 2 and heterogeneously in specimen 3 (fig 10). Pb isotopic signals were retrieved from

318   the interfaces of all three specimens. The background and thermal peak tails corrected $^{207}Pb/^{206}Pb$ ratios

319   are: 0.0900 ± 0.0198 (2σ) for specimen 1, 0.1016 ± 0.0224 (2σ) for specimen 2 and 0.1733 ± 0.0156 (2σ)

320   in specimen 3. Hence, the Pb isotopic signals and calculated $^{207}Pb/^{206}Pb$ ratios for specimens 1 and 2 are

321   identical within error. Specimen 3, however, yields a higher ratio. Calculated model ages for respectively

322   specimens 1, 2 and 3 are 1370 ± 420 Ma (2σ), 1590 ± 420 Ma (2σ) and 2580 ± 150 (2σ). U in the

323   interface was detected as $^{238}UO_2^{++}$ (135 Da). The concentration of U compared to Pb is very low with a

324    $^{238}U/^{206}Pb$ ratio of less than 0.04 in all three specimens. Therefore, it is expected the influence on the

325    $^{207}Pb/^{206}Pb$ ratio is negligible.

326   **Discussion**

327   **Monazite inclusions in rutile**

328   Inclusions typically occur either as a product of exsolution or incorporation during growth. In the rutile

329   studied here, exsolution is unlikely since monazite is present in different host phases (rutile and biotite).

330   The monazite lacks a crystal-preferred orientation that is expected when monazite forms via an exsolution

331   mechanism. Furthermore, P and REE concentrations in rutile are typically very low, with any significant

332   amounts of REE only reported in extra-terrestrial Niobian-rutile (>6 wt. % Nb_2O_5) (Hlava et al., 1972).

333   Therefore, the monazites are interpreted to be primary inclusions trapped within the rutile.

334   The encapsulation of monazite within rutile potentially shields the monazite from external processes

335   (Daneu et al., 2014; Hart et al., 2016; Hart et al., 2018). However, the measured Pb isotopic compositions

336   of monazite at inclusion interfaces are different. The rutile host is characterized by the presence of several

337   twin boundaries and LABs, and these could aid in the diffusion of elements in rutile (Verberne et al.,

338   2022). As shown, some monazite inclusions are in direct contact with these LAB's (Fig 2). Potentially,

339   these inclusions would no longer be fully shielded with trace elements able to migrate out of the rutile-

340   monazite interface. Depending on the timing, inclusions within a single rutile grain could record different

341   isotopic signatures.

342

343   **Formation of trace-element enriched nanoscale clusters**

14

344   **Nanoclusters in the monazite core.** The two types of monazite inclusions are: one with a

345   mottled texture due to radiation damage and one with a distinct core-rim structure (Fig. 4, 5). S/TEM EDS

346   shows that some of the dark and bright spots that lead to the mottled texture are enrichment in Ca, U, and

347   Pb (Fig. 7). The texture and formation of trace element enriched clusters are explained via entrapment in

348   defects generated via radiation damage (Seydoux-Guillaume et al., 2018; Seydoux-Guillaume, 2019). The

349   damaged regions stand out due to structural difference with the host monazite while the bright spot

350   (HAADF) stands out due to being enriched in trace elements, creating this mottled texture as previously

351   observed by others (Seydoux-Guillaume et al., 2019; Turuani et al., 2022; 2023).

352   Clusters within a matrix typically represent a low-energy configuration and are preferable sites for trace

353   elements compared to the crystal lattice of the host. With the rutile present during UHT metamorphism at

354   2580 Ma (Clark et al., 2019), the temperature conditions are met for Pb diffusion into clusters (as

355   observed in Seydoux-Guillaume et al., 2019).

356   The mottled texture therefore is the result of an interplay between the formation and healing of radiation

357   damage sites, and the capture of trace elements in these sites during high-temperature events, which allow

358   for more rapid diffusion of elements.

359   **Nanoscale clusters in the monazite rim.** The rim hosts Ca-rich and Li-rich nanoscale clusters.

360   Given that the lattice of the Ca-rich cluster is the same as the host monazite (Fig 5) with relatively high

361   REE concentrations these clusters are interpreted to be a solid-solution within monazite rather than

362   represent a separate phase.

363   The Li-rich nanoscale cluster has low REE concentrations (<4 at. %) with Li concentrations between 24

364   to 30 at% and P concentrations of ± 10 at. % (fig 9). In the literature, we found no reference for the

365   formation of Li-phosphate in monazite. Nevertheless, the composition of the Li-rich cluster may indicate

366   the formation of a separate Li-phosphate phase.

367   The Mg-rich clusters are only present within the interface and consist of 20 at. % Mg, 10 at% P and, 4

368   at% Ca while showing a depletion in REE concentrations compared to the monazite host. As is the case

369   for the Li-phosphate cluster, the high concentration of Mg suggests the formation of a new phase, via a

370   similar mechanism to the formation of the Ca- and Li-phosphate clusters.

371   **Pb-rich nanoclusters.** Bright spots in HAADF mode associated with the Ca- and Li-rich clusters

372   are rich in Pb based on STEM-EDS (Fig 7). Furthermore, APT based proximity histogram of the Ca- and

373   Li-rich cluster also shows elevated values of Pb. The lack of a ^{204}Pb and ^{208}Pb signal indicated there is no

374   to a negligible ^{232}Th or common Pb component. Potentially, these Pb-rich nanoclusters reflect the same

375   clusters observed within the monazite core. The Pb nanocrystals within the Ca- and Li-phosphate cluster

376   have the same general appearance as Pb present in Si-rich cluster recently described in zircon by (Kusiak.,

377   2015, Kusiak et al., 2019; Lyon et al., 2019), called nanospheres and monazite (Turuani et al., 2022;

378   Turuani et al., 2023) referred to as nanocrystals. Considering we observe a similar presence of Pb in the

379   core that is related associated with U decay, it is unlikely these are primary Pb phases. Furthermore, since

380   we lack data on the structure or valence state of the Pb and associate the Pb with U decay these Pb-rich

381   particles do not fall within the definition of metallic Pb nanospheres (Kusiak 2015, Kusiak et al., 2023).

382   These Pb-rich nanocrystals are intimately linked to the Ca, and Li-rich phosphate clusters, which raises

383   questions about the timing of their formation. One possibility is concurrent formation, with Ca, Li, and Pb

384   migrating at the same time. However, this seems unlikely, as the Pb-rich nanocrystals in the rim are not

385   observed outside of the Ca and Li-rich clusters. If the Pb-rich nanocrystals are indeed the same as those in

386   the core this indicates that during the formation of the rim and the Ca- and Li-rich clusters, the Pb

387   nanocrystals become trapped, preventing small volumes of Pb migrating towards the interface.

388

389   **A Pb mobility model**

390   The texture and compositional variations of the submicron monazite inclusions in rutile provide insight

391   into the tectonothermal history of the studied sample. First, the mottled texture of the monazite (core) is

392   ascribed to both a combination of the presence of radiation damage and the segregation of trace elements

393   into those radiation defects leading to the formation of nanoscale clusters (Seydoux-Guillaume et al.,

394   2019; Seydoux-Guillaume et al., 2002; 2004; 2018; Turuani et al., 2023). Depending on the time of

16

395 monazite growth and the diffusion of trace elements into defects the clusters rich in Pb can be dated if

396 enough time has passed to accumulate radiogenic Pb. This diffusion process is the first stage of trace

397 element mobility.

398 Second, in some of the monazite crystals, the rim yields a different distribution of clusters. The texture

399 indicates partial recrystallization of the monazite rim and encompasses Ca- and Li-phosphate clusters as

400 well as Pb-rich nanocrystals. The presence of a recrystallized rim in only some of the monazite crystals

401 shows that the reaction is localized.

402 Rutile and other repository minerals preserve inclusions due to their low compressibility (Mosenfelder et

403 al., 2005). When exhumed, rutile exerts an overpressure on inclusions (Hart et al., 2016). Differences in

404 compressibility between the rutile host and the inclusions will result in a stress acting upon the monazite

405 (Huang et al., 2010; Zaffiro et al., 2019). Therefore, one explanation could be that the formation of the

406 rim in the monazite is the result of localized stress-induced recrystallization. Alternatively, the presence

407 of Li and to a lesser extent Mg could indicate infiltration of a fluid. This too could cause recrystallization

408 of the monazite rim. In general, rutile is resistant to the infiltration of fluids (Triebold et al., 2007; Zack et

409 al., 2004b). As argued in recent studies on the nanoscale and microstructures in rutile (Verberne et al.,

410 2022; Verberne et al., 2023) the presence of twin boundaries and low-angle boundaries could allow for

411 the transport of trace elements. The same structures potentially facilitate fluid infiltration as well.

412 However, we observe Li primarily in clusters and only minor concentration in the interface itself.

413 Therefore, a localized stress-induced recrystallization appears to fit better with these observations.

414 **Low Th monazite.** The absence or very low concentration of Th in monazite is an odd

415 observation as ThO_2 concentration in monazite are mostly reported to be between $1 – 12$ wt. % (e.g.,

416 Janots et al., 2012, Seydoux-Guillaume et al., 2018). However, a few studies report on monazite with less

417 than 1 wt. % (e.g., Demartin et al.,1991, and Mannucci et al.,1986). Yet, these studies still show

418 measureable amounts of Th. Closest to our observations are a study by Janots et al., 2008. X-ray maps of

419 monazite show a monazite with high Th in the core and a recrystallized rim with low, but not absent, Th

420 concentrations. Although the analyzed rim is 10 mm wide compared to our 100 nm wide rim, and thus

17

421 five orders of magnitude larger. The same underlying principle, recrystallization, would offer an

422 explanation. The recrystallization would have occurred at a low-metamorphic grade Poitrasson et al.,

423 1996, Janots et al. 2008 with Th concentration being positively related to the metamorphic grade

424 (Seydoux 2002). This supports our hypothesis of localized stress-induced recrystallization.

425

426 **Trace element systematics at the rutile-monazite interface**

427 The distribution of trace elements at the interface in specimen 3 is heterogeneous (Fig. 10). In Figure 10

428 lower concentrations of trace elements are observed in the upper part of the boundary compared to the

429 lower part of the boundary. The transition occurs across a domain with linear features rich in trace-

430 elements. These linear features are an expression of dislocations at the interface (Dubosq et al., 2019;

431 Fougerouse et al., 2021b; Verberne et al., 2022; Verberne et al., 2023). Heterogeneities at phase

432 boundaries are commonly observed and well-studied within the material sciences (Larere et al., 1988;

433 Sutton et al., 1995; Suzuki et al., 1991; Suzuki et al., 1981). There is extensive evidence that the degree of

434 trace element segregation has an inverse relationship with the interplanar spacing (Sutton et al., 1995). In

435 iron-alloys, it was found that P migrates to boundaries when this spacing decreases (Suzuki et al., 1981).

436 Also, P and S have different degrees of segregation towards boundaries with different orientations in Ni

437 (Larere et al., 1988) and it is apparent that trace elements segregate in different amounts in function to

438 disorientation in olivine (Tacchetto et al., 2021). The segregation into boundaries for ionic systems is

439 more complex since charge compensation needs to be considered (Kliewer, 1965; Sutton et al., 1995). In

440 TiO_2 Ikeda and Chiang (1993); Ikeda et al. (1993) demonstrated differences in segregation based on the

441 valence states of trace elements e.g., Al^{3+} and Nb^{5+}, boundary type, and the temperature. Here, the

442 curvature of the interface results in a continuous change of opposing crystal faces. Consequently, the

443 spacing between the two phases will vary. This change is reflected in the segregation of trace elements,

444 causing differences in localized trace element concentrations.

445

18

Implications for geochronology: a geological history from submicron monazite inclusions

446 The presence of inclusions with a radiogenic component different from the host mineral can result in a

448 mixed chemical and isotopic system (Fougerouse et al., 2018; Turuani et al., 2022). In this study, Pb is

449 found to have segregated in multiple ways that might have occurred at different moments in time. The

450 clusters still preserved within the monazite core are the result of the interplay between the formation of

451 radiation damage, alpha-healing (Seydoux-Guillaume et al., 2018) and volume diffusion (Seydoux-

452 Guillaume et al., 2019). While recrystallization led to the segregation of Pb from the monazite rim into

453 the rutile-monazite interface. We observe that the recrystallization of the monazite rim is local and not

454 pervasive throughout the rutile grain. Also, we see Pb-enriched nanocrystals trapped within clusters in the

455 recrystallized rim. This localized recrystallization combined with trapping of Pb-enriched nanocrystals

456 would suggest the Pb-enriched features formation and recrystallization occurred in two stages, though

457 without Pb isotopic information from these nanocrystals and the clusters in the core the timing of these

458 stages remains elusive.

459 Regardless, the mobility results in several Pb reservoirs with, potentially unique, Pb isotopic signatures

460 that record the timing of their formation and the decoupling of the U-Pb system. In ideal situations, this

461 Pb signature can be independently studied (Fougerouse et al., 2018; Peterman et al., 2016; Seydoux-

462 Guillaume et al., 2019; Turuani et al., 2022; Valley et al., 2014; Verberne et al., 2020).

463 In this study, the only reservoir with a significant amount of Pb, measurable by APT, is the interface

464 between rutile and monazite. Age determination in APT data is based on analyzing the $^{207}Pb/^{206}Pb$ ratios

465 to derive the timing of Pb segregation in contrast to a direct age. The assumption is that this ratio is

466 preserved after segregation. This also means that the presence of U or Th compared to total Pb needs to be

467 minimal. Important to note is that any additional influx of radiogenic Pb derived from the same source

468 material will obscure the determination of the first event. However, such event could possibly also record

469 the latter, preserving both (Taylor et al., 2023). In our results, the absence of ^{204}Pb and ^{208}Pb supports the

470 assumption that no common Pb is present and thus all Pb is of radiogenic origin (Peterman et al., 2016;

471 Valley et al., 2014; Verberne et al., 2020). The U/Pb ratios in the boundary are <0.05. This indicates large

19

472   amounts of Pb are unsupported and that there is negligible production of radiogenic Pb via continued U

473   decay after the Pb migration into the rim.

474   The ^{207}Pb/^{206}Pb ratio varied between the interfaces in the three APT specimens. The obtained ratios are

475   0.0900 ± 0.0198 (2σ) for specimen 1, 0.1016 ± 0.0224 (2σ) for specimen 2 and 0.1733 ± 0.0156 (2σ) in

476   specimen 3. Specimens 1 and 2 have ^{207}Pb/^{206}Pb ratios with large uncertainties, however, specimen 3

477   yields a more precise ratio which can be evaluated. Let us reiterate that the monazite is enclosed within

478   rutile. Radiogenic is Pb produced by radioactive decay of U and the Pb will be retained in monazite. Later

479   metamorphic and recrystallization events will mobilize the Pb, isolating it from U. Thus the ^{207}Pb/^{206}Pb

480   ratio at the time of Pb segregation is preserved. The rocks in the Napier Complex have a complex history.

481   The oldest potential time of formation is suggested by Black et al., 1984, with monazite crystallization

482   around 3070 Ma. If we assume an initial crystallization age of 3070 Ma, the current ^{207}Pb/^{206}Pb of 0.1733

483   ± 0.0156 (2σ) indicates Pb production for a duration of 2580 Myr before segregation. This would

484   correspond with the decoupling of U-Pb occurring around 550 Ma, which would match the late

485   hydrothermal event in the area (Black, 1983 #18). This shows that analyses of grain boundaries, which

486   are often avoided during geochronological studies can provide additional information about the geological

487   history.

488

496   **ACKNOWLEDGEMENTS**

20

497   The work was conducted within the Geoscience Atom Probe Facility at Curtin University. SMR And

498   DWS acknowledge ARC support. The CLyM (Consortium Lyon St-Etienne de Microscopie) is thanked

499   for access to the TEM NeoARM in Saint-Etienne (France). Stéphanie Reynaud (Université de Saint-

500   Etienne, France) is thanked for her help with FIB sample preparation of one TEM foil. A-M Seydoux-

501   Guillaume thanks the Centre National de la Recherche Scientifique, L'institut National des Sciences de

502   l'Univers (CNRS INSU) for financial support. We would also like to thank Dr. Leanne Staddon and an

503   anonymous reviewer for their constructive feedback.

504   **Conflict of Interest Declarations**

505   The authors declare there are no conflicts of interest.

506

507   **References**

508   Bachmann, F., Hielscher, R., and Schaeben, H., Texture analysis with MTEX–free and open source

509   software toolbox, *in* Proceedings Solid State Phenomena2010, Volume 160, Trans Tech Publ, p.

510   63-68.

511   Bingen, B., and Van Breemen, O., 1998, U-Pb monazite ages in amphibolite-to granulite-facies

512   orthogneiss reflect hydrous mineral breakdown reactions: Sveconorwegian Province of SW

513   Norway: Contributions to Mineralogy and Petrology, v. 132, no. 4, p. 336-353.

514   Black, L., James, P., and Harley, S., 1983, The geochronology, structure and metamorphism of early

515   Archaean rocks at Fyfe Hills, Enderby Land, Antarctica: Precambrian Research, v. 21, no. 3-4, p.

516   197-222.

517   Black, L. P., Fitzgerald, J. D., and Harley, S. L., 1984, Pb isotopic composition, colour, and

518   microstructure of monazites from a polymetamorphic rock in Antarctica: Contributions to

519   Mineralogy and Petrology, v. 85, no. 2, p. 141-148.

520   Black, L., et al. (1986). "Four zircon ages from one rock: the history of a 3930 Ma-old granulite from

521   Mount Sones, Enderby Land, Antarctica." Contributions to Mineralogy and Petrology 94(4): 427-

522   437.

523   Blum, T. B., Darling, J. R., Kelly, T. F., Larson, D. J., Moser, D. E., Perez-Huerta, A., Prosa, T. J.,

524   Reddy, S. M., Reinhard, D. A., and Saxey, D. W., 2018a, Best practices for reporting atom probe

525   analysis of geological materials: Microstructural Geochronology: Planetary Records Down to

526   Atom Scale, v. 232, p. 369-373.

527   Blum, T. B., Reinhard, D. A., Chen, Y., Prosa, T. J., Larson, D. J., and Valley, J. W., 2018b, Uncertainty

528   and Sensitivity Analysis for Spatial and Spectral Processing of Pb Isotopes in Zircon by Atom

529   Probe Tomography: Microstructural Geochronology: Planetary Records Down to Atom Scale, p.

530   327-350.

531   Carson, C. J., Ague, J. J., and Coath, C. D., 2002, U–Pb geochronology from Tonagh Island, East

532   Antarctica: implications for the timing of ultra-high temperature metamorphism of the Napier

533   Complex: Precambrian Research, v. 116, no. 3, p. 237-263.

534   Clark, C., Taylor, R. J., Johnson, T. E., Harley, S. L., Fitzsimons, I. C., and Oliver, L., 2019, Testing the

535   fidelity of thermometers at ultrahigh temperatures: Journal of Metamorphic Geology.

536   Clark, C., Taylor, R. J., Kylander-Clark, A. R., and Hacker, B. R., 2018, Prolonged (> 100 Ma) ultrahigh

537   temperature metamorphism in the Napier Complex, East Antarctica: A petrochronological

538   investigation of Earth's hottest crust: Journal of Metamorphic Geology, v. 36, no. 9, p. 1117-

539   1139.

540   Crameri, F., 2018, Scientific colour maps: Zenodo, v. 10.

541   Dachille, F., Simons, P., and Roy, R., 1968, Pressure-temperature studies of anatase, brookite, rutile and

542   TiO2-II: Am Mineral, v. 53, p. 1929-1939.

543   Daneu, N., Recnik, A., and Mader, W., 2014, Atomic structure and formation mechanism of (101) rutile

544   twins from Diamantina (Brazil): American Mineralogist, v. 99, no. 4, p. 612-624.

545   Demartin, F., Pilati, T., Diella, V., Donzelli, S., & Gramaccioli, C. M. (1991). Alpine monazite; further

546   data. The Canadian Mineralogist, 29(1), 61-67.

547   Dubosq, R., Rogowitz, A., Schweinar, K., Gault, B., and Schneider, D. A., 2019, A 2D and 3D

548   nanostructural study of naturally deformed pyrite: assessing the links between trace element

549   mobility and defect structures: Contributions to Mineralogy and Petrology, v. 174, no. 9, p. 72.

550   Erickson, T., Pearce, M., Taylor, R., Timms, N. E., Clark, C., Reddy, S., and Buick, I., 2015, Deformed

551   monazite yields high-temperature tectonic ages: Geology, v. 43, no. 5, p. 383-386.

552   Fougerouse, D., Reddy, S., Seydoux-Guillaume, A.-M., Kirkland, C., Erickson, T., Saxey, D., Rickard,

553   W., Jacob, D., Leroux, H., and Clark, C., 2021a, Mechanical twinning of monazite expels

554   radiogenic lead: Geology, v. 49, no. 4, p. 417-421.

555   Fougerouse, D., Reddy, S. M., Aylmore, M., Yang, L., Guagliardo, P., Saxey, D. W., Rickard, W. D., and

556   Timms, N., 2021b, A new kind of invisible gold in pyrite hosted in deformation-related

557   dislocations: Geology, v. 49, no. 10, p. 1225-1229.

558   Fougerouse, D., Reddy, S. M., Saxey, D. W., Erickson, T. M., Kirkland, C. L., Rickard, W. D. A.,

559   Seydoux-Guillaume, A. M., Clark, C., and Buick, I. S., 2018, Nanoscale distribution of Pb in

560   monazite revealed by atom probe microscopy: Chemical Geology, v. 479, p. 251-258.

561   Fougerouse, D., Saxey, D. W., Rickard, W. D., Reddy, S. M., and Verberne, R., 2021c, Standardizing

562   Spatial Reconstruction Parameters for the Atom Probe Analysis of Common Minerals:

563   Microscopy and Microanalysis, p. 1-10.

564   Grand'Homme, A., Janots, E., Seydoux-Guillaume, A.-M., Guillaume, D., Bosse, V., and Magnin, V.,

565   2016, Partial resetting of the U-Th-Pb systems in experimentally altered monazite: Nanoscale

566   evidence of incomplete replacement: Geology, v. 44, no. 6, p. 431-434.

567   Harley, S. L., 2016, A matter of time: the importance of the duration of UHT metamorphism: Journal of

568   Mineralogical and Petrological Sciences, v. 111, no. 2, p. 50-72.

569 Harley, S. L., and Motoyoshi, Y., 2000, Al zoning in orthopyroxene in a sapphirine quartzite: evidence

570   for> 1120 C UHT metamorphism in the Napier Complex, Antarctica, and implications for the

571   entropy of sapphirine: Contributions to Mineralogy and Petrology, v. 138, no. 4, p. 293-307.

572 Harley, S. L., & Black, L. P. (1987). The Archaean geological evolution of Enderby Land, Antarctica. In

573   R. G. Park & J. Tarney (Eds.), Evolution of the Lewisian and comparable Precambrian high grade

574   terrains (27th edn, pp. 285–296). Oxford: Geological Society of London.

575 Hart, E., Storey, C., Bruand, E., Schertl, H. P., and Alexander, B. D., 2016, Mineral inclusions in rutile: A

576   novel recorder of HP-UHP metamorphism: Earth and Planetary Science Letters, v. 446, p. 137-

577   148.

578 Hart, E., Storey, C., Harley, S. L., and Fowler, M., 2018, A window into the lower crust: Trace element

579   systematics and the occurrence of inclusions/intergrowths in granulite-facies rutile: Gondwana

580   Research, v. 59, p. 76-86.

581 Hellman, O. C., Vandenbroucke, J. A., Rusing, J., Isheim, D., and Seidman, D. N., 2000, Analysis of

582   Three-dimensional Atom probe Data by the Proximity Histogram: Microsc Microanal, v. 6, no. 5,

583   p. 437-444.

584 Hlava, P., Prinz, M., and Keil, K., 1972, Niobian rutile in an Apollo 14 KREEP fragment: Meteoritics, v.

585   7, no. 4, p. 479-486.

586 Hokada, T., 2001, Feldspar thermometry in ultrahigh-temperature metamorphic rocks: Evidence of crustal

587   metamorphism attaining~ 1100 C in the Archean Napier Complex, East Antarctica: American

588   Mineralogist, v. 86, no. 7-8, p. 932-938.

589 Huang, T., Lee, J.-S., Kung, J., and Lin, C.-M., 2010, Study of monazite under high pressure: Solid State

590   Communications, v. 150, no. 37-38, p. 1845-1850.

591 Ikeda, J. A. S., and Chiang, Y. M., 1993, Space charge segregation at grain boundaries in titanium

592   dioxide: I, relationship between lattice defect chemistry and space charge potential: Journal of the

593   American Ceramic Society, v. 76, no. 10, p. 2437-2446.

594 Ikeda, J. A. S., Chiang, Y. M., Garratt-Reed, A. J., and Sande, J. B. V., 1993, Space charge segregation at

595   grain boundaries in titanium dioxide: II, model experiments: Journal of the American Ceramic

596   Society, v. 76, no. 10, p. 2447-2459.

597 James, P., and Black, L., 1981, Archaean Geology.

598 Janots, E., Berger, A., Gnos, E., Whitehouse, M., Lewin, E., & Pettke, T. (2012). Constraints on fluid

599   evolution during metamorphism from U–Th–Pb systematics in Alpine hydrothermal monazite.

600   Chemical Geology, 326, 61-71.

601 Janots, E., Engi, M., Berger, A., Allaz, J., Schwarz, J. O., & Spandler, C. (2008). Prograde metamorphic

602   sequence of REE minerals in pelitic rocks of the Central Alps: implications for allanite–

603   monazite–xenotime phase relations from 250 to 610 C. *Journal of Metamorphic Geology*, *26*(5),

604   509-526.

605 Kliewer, K., 1965, Space charge in ionic crystals. II. The electron affinity and impurity accumulation:

606   Physical Review, v. 140, no. 4A, p. A1241.

607 Kooijman, E., Mezger, K., and Berndt, J., 2010, Constraints on the U-Pb systematics of metamorphic

608   rutile from in situ LA-ICP-MS analysis: Earth and Planetary Science Letters, v. 293, no. 3-4, p.

609   321-330.

610 Kusiak, M., Kovaleva, E., Wirth, R., Klötzli, U., Dunkley, D., Yi, K., and Lee, S., 2019, Lead oxide

611   nanospheres in seismically deformed zircon grains: Geochimica et Cosmochimica Acta, v. 262, p.

612   20-30.

613 Larere, A., Guillope, M., and Masuda-Jindo, K., 1988, Segregation energies of phosphorus and sulfur in

614   various relaxed structures of grain boundaries in Ni by tight-binding approximation: Le Journal

615   de Physique Colloques, v. 49, no. C5, p. C5-447-C445-450.

616 Lloyd, G. E., Farmer, A. B., and Mainprice, D., 1997, Misorientation analysis and the formation and

617   orientation of subgrain and grain boundaries: Tectonophysics, v. 279, no. 1-4, p. 55-78.

618 Lyon, I., Kusiak, M., Wirth, R., Whitehouse, M., Dunkley, D., Wilde, S., Schaumlöffel, D., Malherbe, J.,
619   and Moore, K., 2019, Pb nanospheres in ancient zircon yield model ages for zircon formation and
620   Pb mobilization: Scientific Reports, v. 9.

621 Mannucci, G., Diella, V., Gramaccioli, C. M., & Pilati, T. (1986). A comparative study of some
622   pegmatitic and fissure monazite from the Alps. The Canadian Mineralogist, 24(3), 469-474.

623 Meinhold, G., 2010, Rutile and its applications in earth sciences: Earth-Science Reviews, v. 102, no. 1-2,
624   p. 1-28.

625 Mitchell, R. J., and Harley, S. L., 2017, Zr-in-rutile resetting in aluminosilicate bearing ultra-high
626   temperature granulites: Refining the record of cooling and hydration in the Napier Complex,
627   Antarctica: Lithos, v. 272, p. 128-146.

628 Mosenfelder, J. L., Schertl, H.-P., Smyth, J. R., and Liou, J. G., 2005, Factors in the preservation of
629   coesite: The importance of fluid infiltration: American Mineralogist, v. 90, no. 5-6, p. 779-789.

630 Ni, Y., Hughes, J. M., and Mariano, A. N., 1995, Crystal chemistry of the monazite and xenotime
631   structures: American Mineralogist, v. 80, no. 1-2, p. 21-26.

632 Pape, J., Mezger, K., and Robyr, M., 2016, A systematic evaluation of the Zr-in-rutile thermometer in
633   ultra-high temperature (UHT) rocks: Contributions to Mineralogy and Petrology, v. 171, no. 5.

634 Peterman, E. M., Reddy, S. M., Saxey, D. W., Snoeyenbos, D. R., Rickard, W. D., Fougerouse, D., and
635   Kylander-Clark, A. R., 2016, Nanogeochronology of discordant zircon measured by atom probe
636   microscopy of Pb-enriched dislocation loops: Sci Adv, v. 2, no. 9, p. e1601318.

637 Poitrasson, F., Chenery, S., & Bland, D. J. (1996). Contrasted monazite hydrothermal alteration
638   mechanisms and their geochemical implications. Earth and Planetary Science Letters, 145(1-4),
639   79-96.

640 Prior, D. J., Wheeler, J., Peruzzo, L., Spiess, R., and Storey, C., 2002, Some garnet microstructures: an
641   illustration of the potential of orientation maps and misorientation analysis in microstructural
642   studies: Journal of Structural Geology, v. 24, no. 6-7, p. 999-1011.

643 Reddy, S. M., Saxey, D. W., Rickard, W. D., Fougerouse, D., Montalvo, S. D., Verberne, R., and Van

644   Riessen, A., 2020, Atom Probe Tomography: Development and Application to the Geosciences:

645   Geostandards and Geoanalytical Research, v. 44, no. 1, p. 5-50.

646 Reddy, S. M., Timms, N. E., Pantleon, W., and Trimby, P., 2007, Quantitative characterization of plastic

647   deformation of zircon and geological implications: Contributions to Mineralogy and Petrology, v.

648   153, no. 6, p. 625-645.

649 Rickard, W. D., Reddy, S. M., Saxey, D. W., Fougerouse, D., Timms, N. E., Daly, L., Peterman, E.,

650   Cavosie, A. J., and Jourdan, F., 2020, Novel Applications of FIB-SEM-Based ToF-SIMS in Atom

651   Probe Tomography Workflows: Microscopy and Microanalysis, p. 1-8.

652 Seydoux-Guillaume, A.-M., Fougerouse, D., Laurent, A., Gardés, E., Reddy, S., and Saxey, D., 2019,

653   Nanoscale resetting of the Th/Pb system in an isotopically-closed monazite grain: A combined

654   atom probe and transmission electron microscopy study: Geoscience Frontiers, v. 10, no. 1, p. 65-

655   76.

656 Seydoux-Guillaume A.-M., Deschanels X., Baumier C., Neumeier S., Weber W.J., and Peuget S. (2018).

657   Why natural monazite never becomes amorphous: experimental evidence for alpha self-healing.

658   *American Mineralogist, 103, 824-827. doi.org/10.2138/am-2018-6447*

659 Seydoux-Guillaume A.M., Wirth R., Deutsch A. and Schärer U. (2004). Microstructure of 24 – 1928 Ma

660   concordant monazites: implications for geochronology and nuclear waste deposits. *Geoch.*

661   *Cosmochim. Acta*, Vol. 68, 2517-2527.

662 Seydoux-Guillaume, A.-M., Montel, J.-M., Bingen, B., Bosse, V., De Parseval, P., Paquette, J.-L., Janots,

663   E., and Wirth, R., 2012, Low-temperature alteration of monazite: Fluid mediated coupled

664   dissolution–precipitation, irradiation damage, and disturbance of the U–Pb and Th–Pb

665   chronometers: Chemical Geology, v. 330, p. 140-158.

666 Seydoux-Guillaume A.M., Goncalves P., Wirth R. and Deutsch A. (2003). TEM study of polyphasic and

667   discordant monazites: site specific specimen preparation using the Focused Ion Beam technique.

668   *Geology,* Vol. 31, 973-976.

669   Seydoux-Guillaume A.M., Wirth R., Nasdala L., Gottschalk M., Montel J.M. and Heinrich W. (2002b).

670   An XRD, TEM and Raman study of experimentally annealed natural monazite. *Phys. Chem.*

671   *Minerals*, Vol. 29, 240-253.

672   Seydoux-Guillaume, A.-M., Paquette, J.-L., Wiedenbeck, M., Montel, J.-M., and Heinrich, W., 2002,

673   Experimental resetting of the U–Th–Pb systems in monazite: Chemical geology, v. 191, no. 1-3,

674   p. 165-181.

675   Seydoux-Guillaume A.M., Wirth R., Heinrich W. and Montel J.M. (2002). Experimental determination

676   of the Th partitioning between monazite and xenotime using Analytical Electron Microscopy and

677   X-ray Diffraction Rietveld analysis. Eur. J. Mineral., Vol. 14, 869 — 878.

678   Sheraton, J. W., Thomson, J. W., and Collerson, K. D., Mafic dyke swarms of Antarctica1987,

679   Geological Association of Canada.

680   Smye, A. J., and Stockli, D. F., 2014, Rutile U-Pb age depth profiling: A continuous record of

681   lithospheric thermal evolution: Earth and Planetary Science Letters, v. 408, p. 171-182.

682   Sutton, A. P., Balluffi, R. W., and Sutton, A., 1995, Interfaces in crystalline materials.

683   Suzuki, K., Ichihara, M., and Takeuchi, S., 1991, High-resolution electron microscopy of lattice defects in

684   TiO2 and SnO2: Philosophical Magazine A, v. 63, no. 4, p. 657-665.

685   Suzuki, S., Abiko, K., and Kimura, H., 1981, Phosphorus segregation related to the grain boundary

686   structure in an Fe☐P alloy: Scripta Metallurgica, v. 15, no. 10, p. 1139-1143.

687   Swope, R. J., Smyth, J. R., and Larson, A. C., 1995, H in rutile-type compounds: I. Single-crystal neutron

688   and X-ray diffraction study of H in rutile: American Mineralogist, v. 80, no. 5-6, p. 448-453.

689   Tacchetto, T., Reddy, S. M., Saxey, D. W., Fougerouse, D., Rickard, W. D. A., and Clark, C., 2021,

690   Disorientation control on trace element segregation in fluid-affected low-angle boundaries in

691   olivine: Contributions to Mineralogy and Petrology, v. 176, no. 7, p. 59.

692   Taylor, R. J., Reddy, S. M., Saxey, D. W., Rickard, W. D., Tang, F., Borlina, C. S., Fu, R. R., Weiss, B.

693   P., Bagot, P., and Williams, H. M., 2023, Direct age constraints on the magnetism of Jack Hills

694   zircon: Science Advances, v. 9, no. 1, p. eadd1511.

695   Thompson, K., Lawrence, D., Larson, D. J., Olson, J. D., Kelly, T. F., and Gorman, B., 2007, In situ site-

696   specific specimen preparation for atom probe tomography: Ultramicroscopy, v. 107, no. 2-3, p.

697   131-139.

698   Triebold, S., von Eynatten, H., Luvizotto, G. L., and Zack, T., 2007, Deducing source rock lithology from

699   detrital rutile geochemistry: An example from the Erzgebirge, Germany: Chemical Geology, v.

700   244, no. 3-4, p. 421-436.

701   Turuani, M. J., Laurent, A. T., Seydoux-Guillaume, A. M., Fougerouse, D., Saxey, D., Reddy, S. M.,

702   Harley, S. L., Reynaud, S., and Rickard, W. D. A., 2022, Partial retention of radiogenic Pb in

703   galena nanocrystals explains discordance in monazite from Napier Complex (Antarctica): Earth

704   and Planetary Science Letters, v. 588.

705   Turuani, M. J., Seydoux-Guillaume, A.-M., Laurent, A. T., Reddy, S., Harley, S., Fougerouse, D., Saxey,

706   D., Gouy, S., Parseval, D., and Reynaud, S., 2023, Nanoscale features revealed by a multiscale

707   characterization of discordant monazite highlight mobility mechanisms of Th and Pb.

708   Valley, J. W., Cavosie, A. J., Ushikubo, T., Reinhard, D. A., Lawrence, D. F., Larson, D. J., Clifton, P.

709   H., Kelly, T. F., Wilde, S. A., and Moser, D. E., 2014, Hadean age for a post-magma-ocean

710   zircon confirmed by atom-probe tomography: Nature Geoscience, v. 7, no. 3, p. 219-223.

711   Verberne, R., Reddy, S., Saxey, D., Fougerouse, D., Rickard, W., Plavsa, D., Agangi, A., and Kylander-

712   Clark, A., 2020, The geochemical and geochronological implications of nanoscale trace-element

713   clusters in rutile: Geology.

714   Verberne, R., Reddy, S. M., Saxey, D. W., Fougerouse, D., Rickard, W. D., Quadir, Z., Evans, N. J., and

715   Clark, C., 2022, Dislocations in minerals: Fast-diffusion pathways or trace-element traps?: Earth

716   and Planetary Science Letters, v. 584, p. 117517.

717   Verberne, R., Saxey, D. W., Reddy, S. M., Rickard, W. D., Fougerouse, D., and Clark, C., 2019, Analysis

718   of Natural Rutile (TiO2) by Laser-assisted Atom Probe Tomography: Microscopy and

719   Microanalysis, p. 1-8.

720   Verberne, R., van Schrojenstein Lantman, H. W., Reddy, S. M., Alvaro, M., Wallis, D., Fougerouse, D.,

721   Langone, A., Saxey, D. W., and Rickard, W. D., 2023, Trace-element heterogeneity in rutile

722   linked to dislocation structures: Implications for Zr-in-rutile geothermometry: Journal of

723   Metamorphic Geology, v. 41, no. 1, p. 3-24.

724   Watson, E. B., Wark, D. A., and Thomas, J. B., 2006, Crystallization thermometers for zircon and rutile:

725   Contributions to Mineralogy and Petrology, v. 151, no. 4, p. 413-433.

726   Zack, T., Moraes, R., and Kronz, A., 2004a, Temperature dependence of Zr in rutile: empirical calibration

727   of a rutile thermometer: Contributions to Mineralogy and Petrology, v. 148, no. 4, p. 471-488.

728   Zack, T., von Eynatten, H., and Kronz, A., 2004b, Rutile geochemistry and its potential use in

729   quantitative provenance studies: Sedimentary Geology, v. 171, no. 1-4, p. 37-58.

730   Zaffiro, G., Angel, R. J., and Alvaro, M., 2019, Constraints on the Equations of State of stiff anisotropic

731   minerals: rutile, and the implications for rutile elastic barometry: Mineralogical Magazine, v. 83,

732   no. 3, p. 339-347.

733

734   **Figure captions**

735   **Fig. 1** a) Simplified geological map of the Napier complex after (Carson et al., 2002). b)

736   Photomicrography showing the location of the analyzed rutile grain within the thin section. The rutile is

737   in contact with a coarse garnet that hosts rutile, spinel and sapphirine inclusions and resides in a matrix of

738   mesoperthite, quartz and minor biotite. C and d) Field images of the outcrop at Mt. Hardy. The photos

739   show the large scale foliation present at the sample locality with close up photo of a <u>leucosome</u> rich in

740   coarse-grained <u>garnet</u> and quartz from which the sample was prepared. Sample coordinates 66°49'04.2"S

741   50°42'60.0"E. Fsp = feldspar, Grt = garnet, Sph = sapphirine, Sp = spinel, Rt = rutile, Msp =

742   mesoperthite. Red arrow indicates studied rutile.

743   **Fig. 2:** (a): BSE images of analyzed rutile (Rt). Rutile is surrounded garnet (Grt), mesoperthite (Msp), k-

744   feldspar (Kfs) and biotite (Bt). The lift-out locations for TEM and APT specimens are indicated on the

745   image. TEM-1 corresponds to the lift-out taken at Curtin University and this monazite has a recrystallized

746   rim. TEM-2 corresponds with the monazite that does not show the recrystallized rim (b): BSE image

747   showing the presence of the submicron monazites (Mnz) in rutile, as well as corundum (Crn) and Fe-

748   oxide exsolutions. (c): BSE image of biotite directly in contact with rutile, also hosting submicron

749   monazite. (d) Mean-misorientation map showing the subtle differences in orientations that are linked to

750   low-angle boundaries. The black boundaries show the location of twin boundaries (cf. (Verberne et al.,

751   2022)). (e) Mean-misorientation and local misorientation maps for two low-angle boundaries. In both

752   maps a monazite is present, with LAB 1 being in close vicinity and LAB 2 being pinned on the monazite

753   inclusion. The corresponding slip system for the low-angle boundaries is {101]<201>.

754

755   **Fig 3.** TEM BF cross-section to illustrate the structure of the monazite inclusion. From outward inward:

756   the rutile host, the interface between rutile and the monazite, the recrystallized rim including 5-20nm

757   clusters and nano-inclusions of Li, Ca and Pb, and the core of the monazite exhibiting a mottled texture.

31

758 **Fig. 4:** TEM/STEM characterization of the TEM foils. a) From the left to the right: TEM-Bright Field

759 (BF) image of one entire monazite inclusion in rutile, Selected Area Electron Diffraction (SAED) pattern

760 from the monazite inclusion seen in the [12-1] zone axis and associated with a crystallographic model

761 from $CePO_4$-monazite in the same orientation, and high-resolution STEM-Annular Dark Field (ADF)

762 image of the monazite-rutile interface. b-Top) Left STEM-ADF and right STEM-ABF images from part

763 of the Mnz inclusion seen in A. b-below) STEM BF and HAADF images from a Mnz inclusion with an

764 alteration rim.

765 **Fig. 5 STEM-ADF images** of clusters in the core and recrystallization rim. a-c) within the core there is a

766 high density of clusters (bright spots) which are trapped within zones of radiation damage (black spots).

767 d-f) The recrystallized rim yields far fewer bright spots, however different inclusions are visible. Note

768 that despite the presence of clusters and inclusions the lattice is almost not affected

769 **Fig 6:** Mass spectrum of rutile, monazite and the interface with highlighted trace elements that are

770 enriched in the interface. Li, Ca and U are observed in one location in the mass spectrum. Pb is observed

771 at both Pb^+ and Pb^{++}. ^{206}Pb is visible at 103 Da and 206 Da, and ^{207}Pb is observed at 103.5 Da and 207 Da,

772 ^{208}Pb is not present above background.

773

774 **Fig 7: TEM EDS spectra and maps**

775 a) TEM EDS analyses conducted on a monazite without recrystallized rim. EDS analyses was performed

776 on the matrix and a cluster to show the difference in composition and the presence of Ca, Pb and U in the

777 cluster. b) TEM EDS maps of the core of the monazite with a recrystallized rim showing the clusters are

778 rich in Ca, Pb, and U. c) TEM EDS maps of clusters present in the recrystallized rim. Ce is shown as an

779 indication for decreased concentrations of major elements. d) TEM EDS interface analysis, showing an

780 EDS map to highlight that Pb is enriched at the interface with a Pb concentration profile (white arrow).

781 **Fig. 8** (a, b): Ion maps of specimen 1 and 2 showing monazite (green) is encapsulated within rutile (grey).

782 The interface is enriched in Ca and Pb in both specimens. Also, the curvature over the monazite interface

783   is clearly visible in the ion maps of specimen 2. (c): Ion maps of specimen 3 not only yields a Pb and Ca

784   enriched interface but also reveal the presence of Ca (d) and Li-rich (e) inclusions. Within the Li-rich

785   inclusion an isoconcentration surface for Pb is shown to demonstrate the presence and equivalence of the

786   inclusions in Fig 4b

787

788   **Fig 9** a) Proximity histograms for the three inclusions observed within the APT data. All inclusions show

789   a slight increase in Pb concentration and a strong increase in one of three cations (Ca, Li, Mg) indicating

790   the formation of a new phase or solid-solution. Ce is shown as a proxy for the REE, which show similar

791   trends at lower concentrations.

792

793   **Fig. 10** Ion map showing the heterogeneous distribution of Si + Al within the interface of specimen 3.

794   The 1D concentration profile was taken along the interface as indicated in the top panel. The enrichment

795   of Al, Si and Pb clearly various within each section. The linear features near the middle are interpreted as

796   dislocation present at the interface

797

798

799

800

801

802

803

804

33
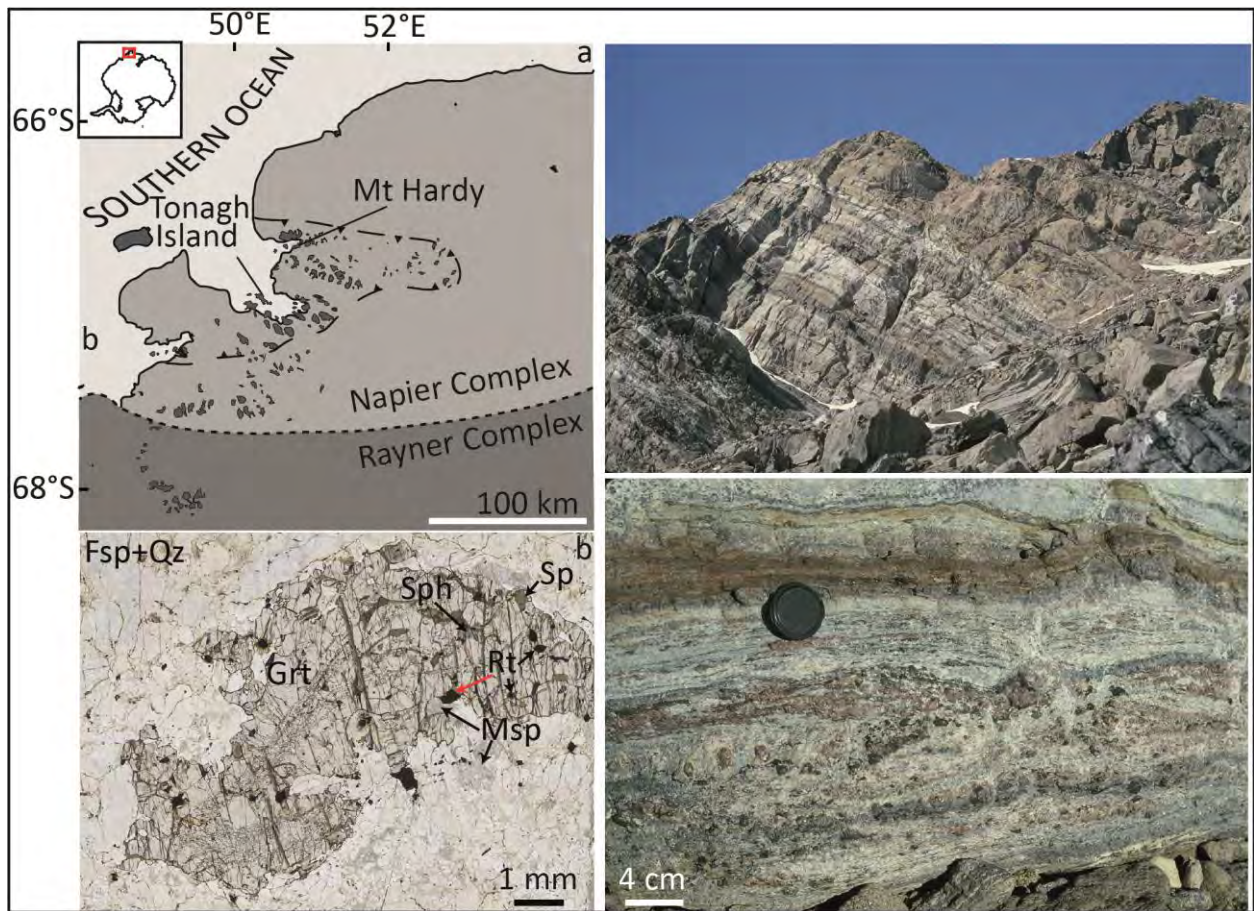
805   Figure 1

806

807

808

809

810

811

812

813

814

815   Figure 2
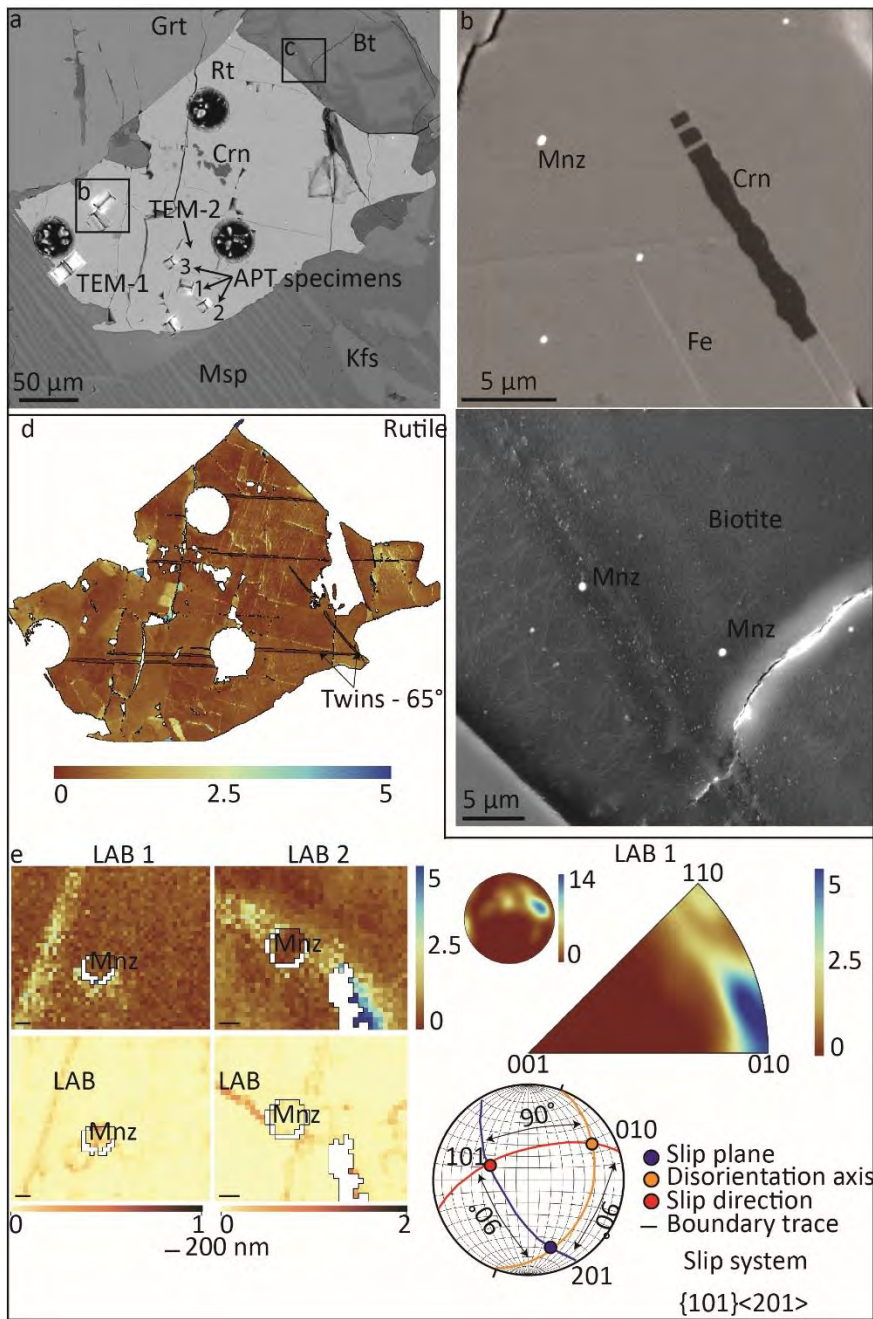
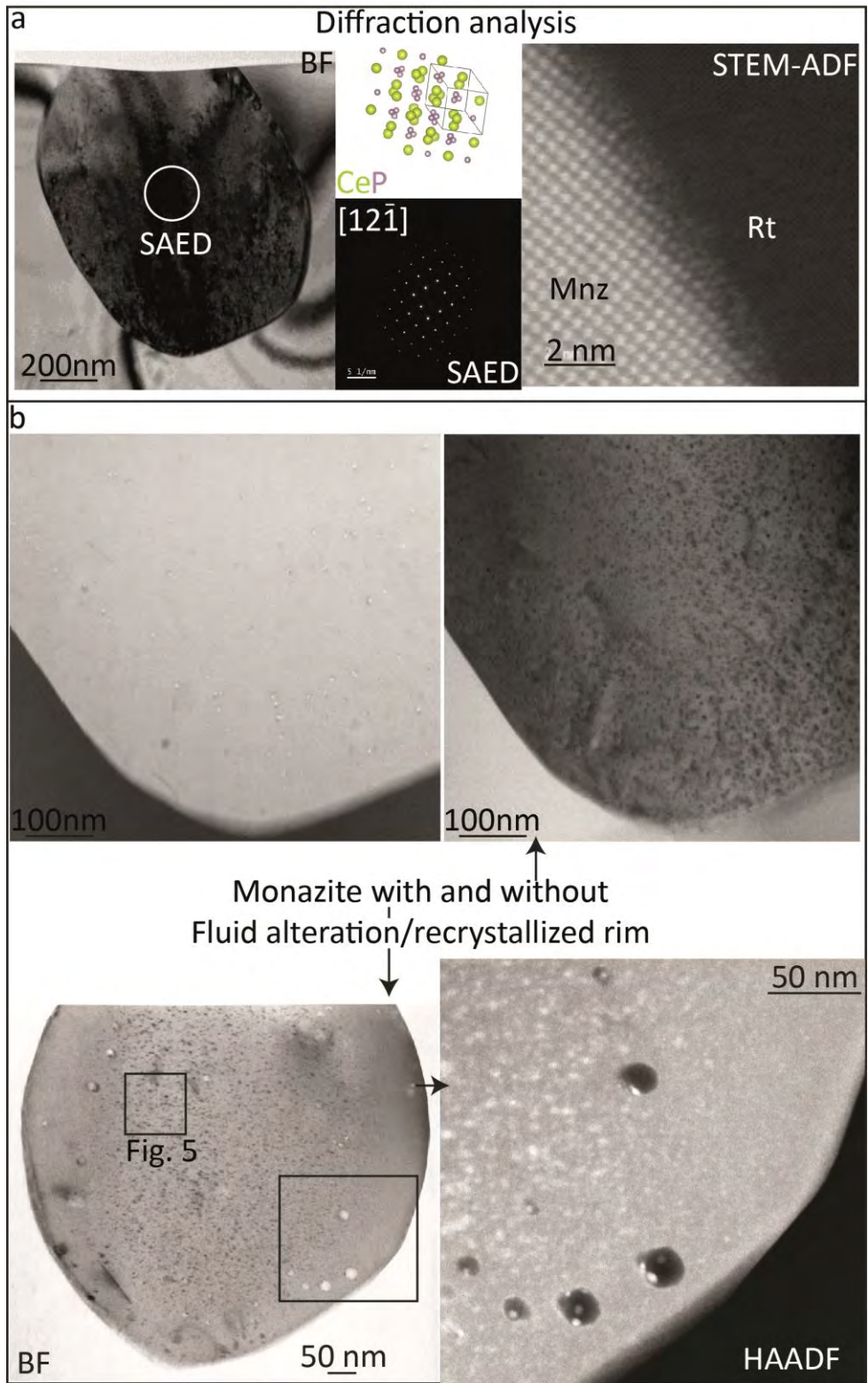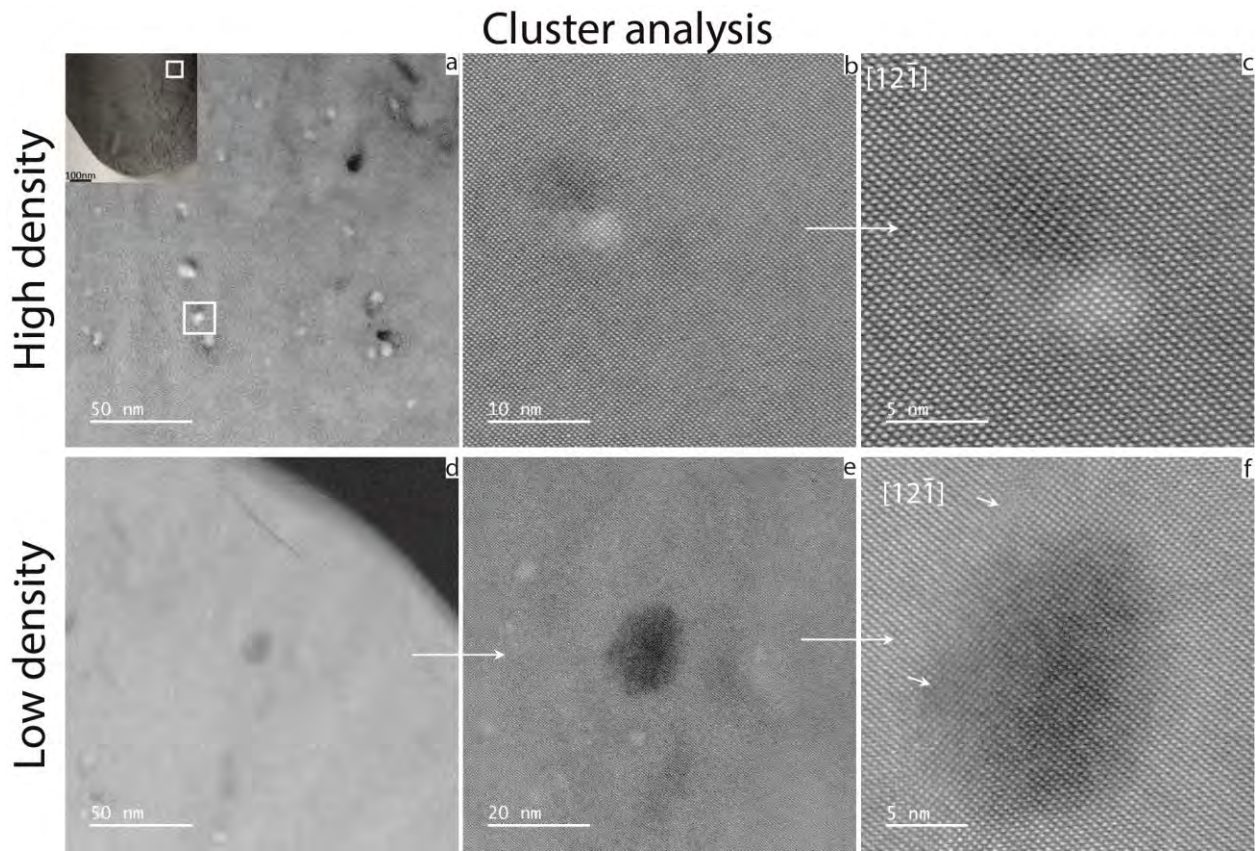816

817

818

819

820   Figure 3

821

822
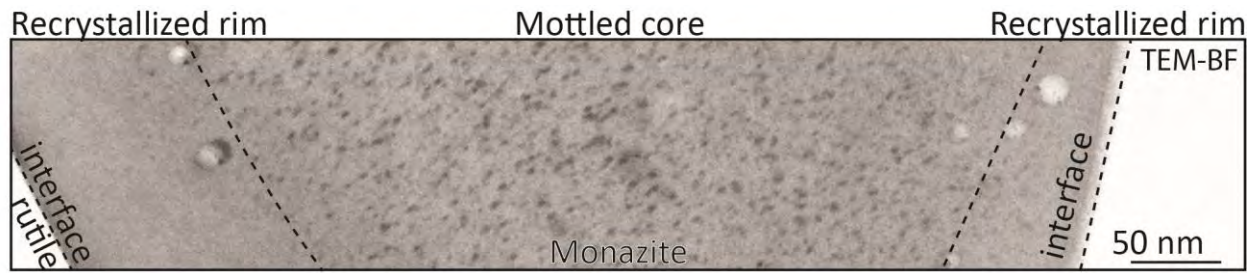
823   Figure 4

824

825   Figure 5

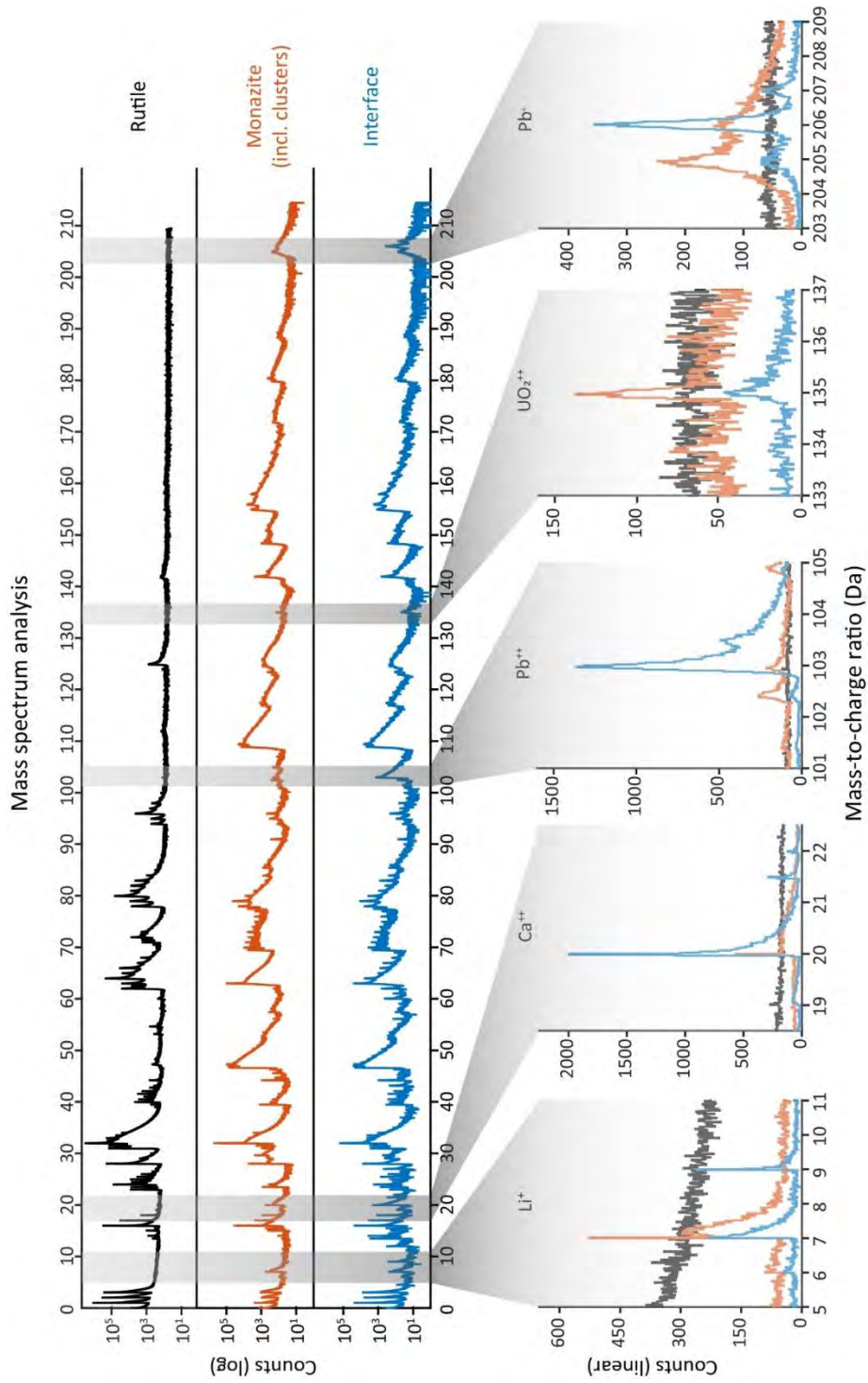

826

827

828   Figure 6

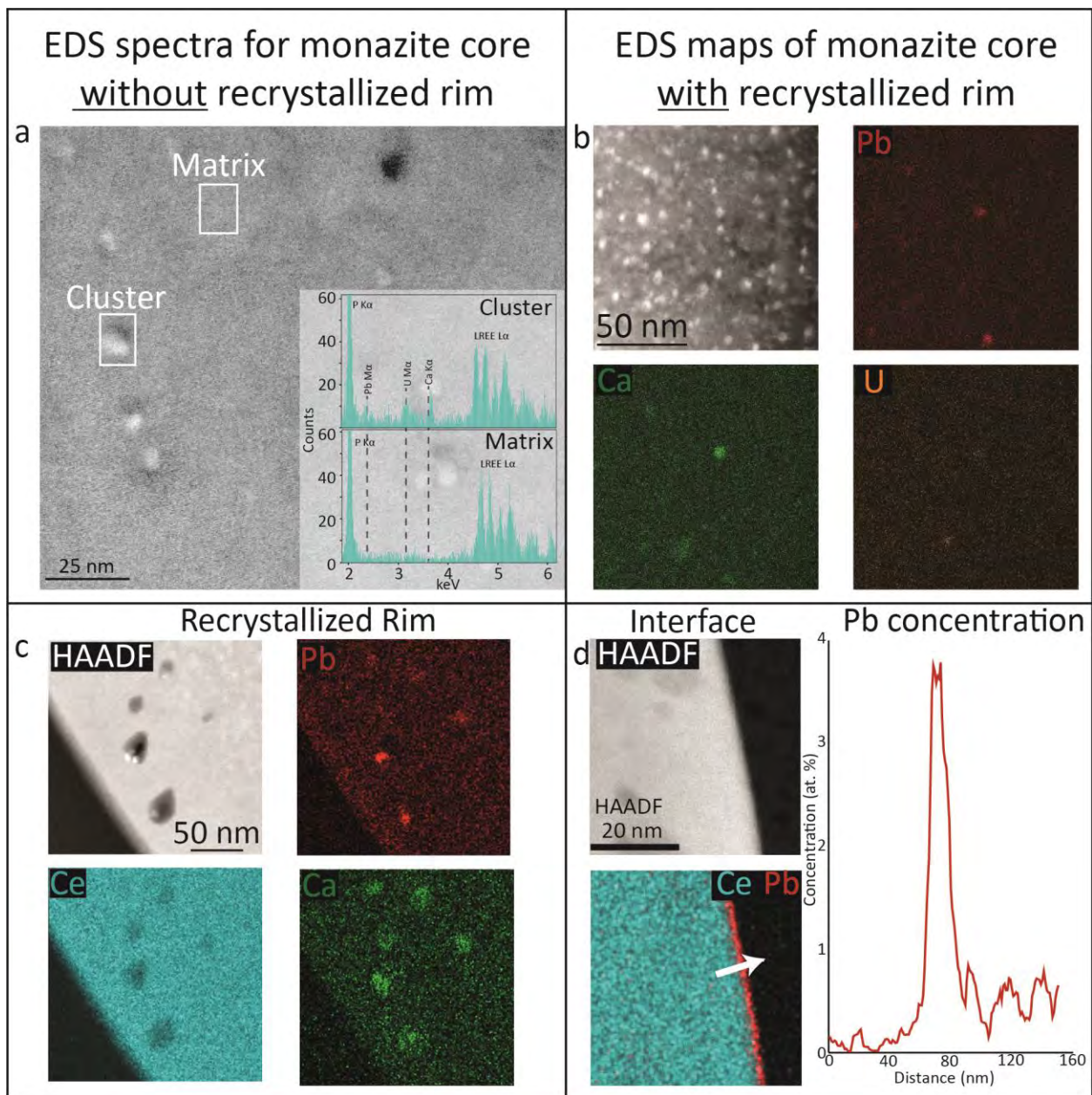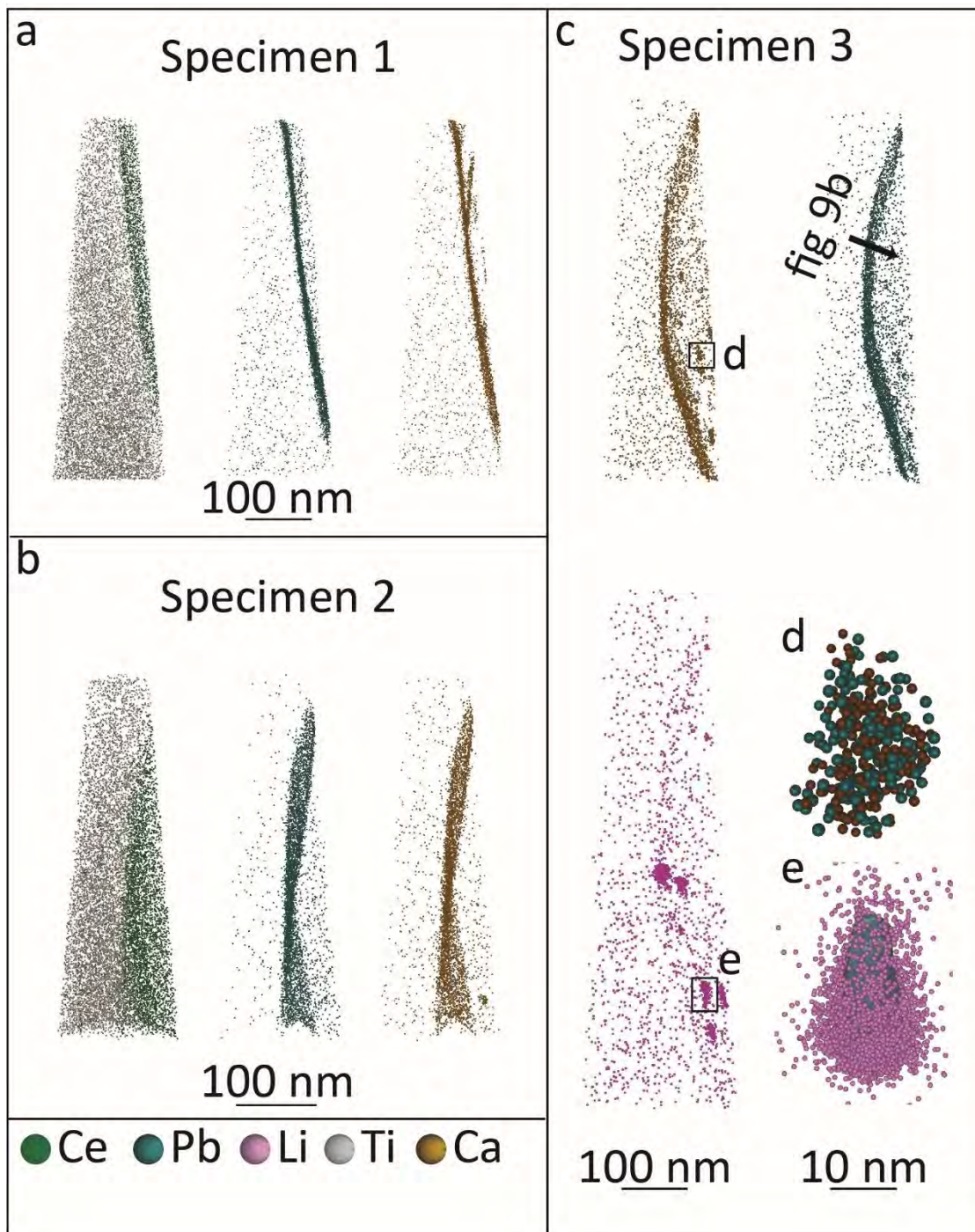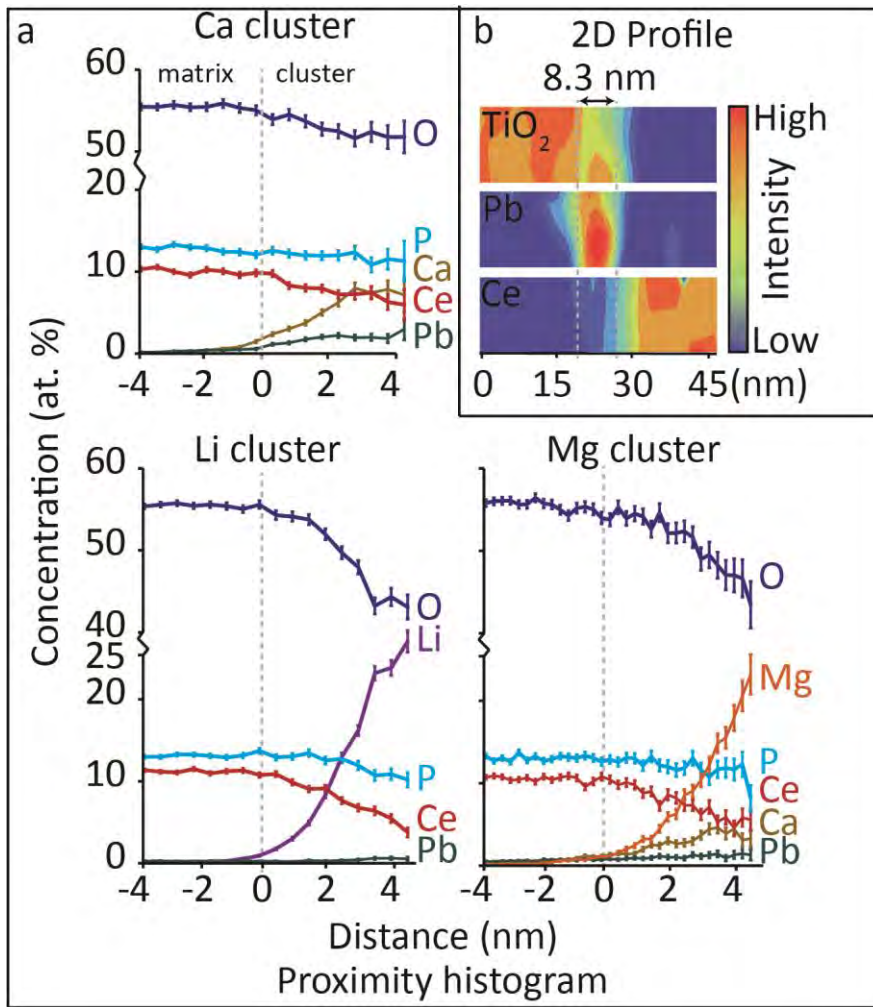829

830
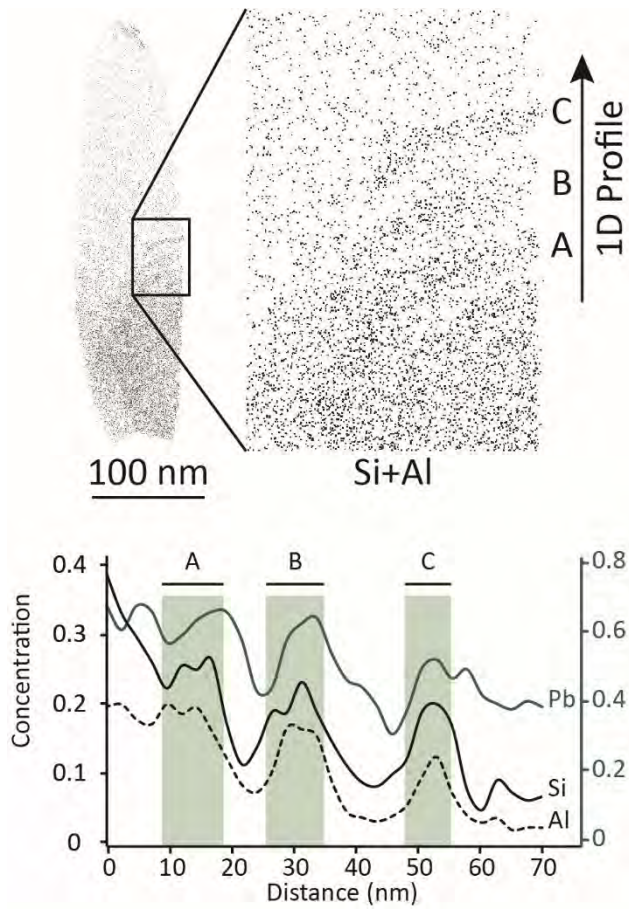
831

39

832   Figure 7

833

834

835

836

837   Figure 8

838

839

840   Figure 9

841

842

843   Figure 10

844